is responsible for *TAL1* overexpression in these cells. Furthermore, ChIP-seq for H3K27ac showed complete collapse of the super-enhancer at the *TAL1* locus when the deletion affected the allele with the enhancer mutation but was not affected when the deletion involved only the wild-type allele (Fig. 4B and figs. S8 and S9).

We also targeted a single guide RNA to specific sequences that form part of the 12-bp insertion in Jurkat cells, which permitted us to propagate single-cell clones with a spectrum of repair-induced indel mutations directly at the insertion site (Fig. 4C). In clones with deletion of 6 bp of the 12-bp enhancer insertion, encompassing one of the two inserted MYB binding sites, endogenous TAL1 expression levels decreased by ~60%, whereas clones with more extensive deletions had endogenous TAL1 expression levels decreased by ~85% (Fig 4C). Thus, the MuTE is clearly responsible for TAL1 overexpression in Jurkat cells.

Our ChIP-seq results also show that MYB and CBP were bound together at 727 of the 818 (89%) super-enhancer regions that are present in Jurkat cells. When we performed short hairpin RNA–mediated knockdown for MYB, 221 of 818 (27%) super-enhancer–associated genes decreased significantly in expression (*9*, *17*), which suggested that MYB has an active role in regulating their transcription. These results are consistent with the interpretation that MYB-CBP binding and the subsequent formation of abundant H3K27 acetylation marks may be broadly involved in the formation of super-enhancers in T-ALL. Thus, the role that we have shown for MYB binding in super-enhancer formation in a subset of T-ALLs with strategically placed somatic indel mutations in all likelihood provides insight into the general question of how super-enhancers are formed at the site of genes critical for the establishment of the T-ALL cell state. MYB is known to function as a master regulator of early and adult hematopoiesis and to undergo transcriptional down-regulation after lineage commitment and differentiation (*22*). An interesting area for future study will be to determine whether MYB acts in concert with CBP to regulate super-enhancer formation at genes critical for defining cell identity during normal hematopoietic cell differentiation (*14*, *16*, *23*, *24*).

Our findings show that somatic mutation of noncoding intergenic elements can lead to binding of master transcription factors, such as MYB, which in turn aberrantly initiate super-enhancers that mediate overexpression of oncogenes. This raises the possibility that acquisition of such enhancer mutations may constitute a general mechanism of carcinogenesis used in other types of human cancers. Mechanisms of aberrant super-enhancer formation in malignancy have broad implications not only for molecular pathogenesis but also for clinical management. Drugs that target key components of the transcriptional machinery, such as BRD4 and CDK7 (*12*, *13*, *17*), have recently been shown to preferentially target tumor-specific super-enhancers, which provides a novel strategy to capitalize on these abnormalities for improved cancer therapy.

REFERENCES AND NOTES

1. E. J. Walker *et al.*, *Cancer Res.* **72**, 636–644 (2012).
2. A. Gimelbrant, J. N. Hutchinson, B. R. Thompson, A. Chess, *Science* **318**, 1136–1140 (2007).
3. R. L. Jirtle, *Exp. Cell Res.* **248**, 18–24 (1999).
4. T. M. Breit *et al.*, *J. Exp. Med.* **177**, 965–977 (1993).
5. L. Brown *et al.*, *EMBO J.* **9**, 3343–3351 (1990).
6. P. D. Aplan *et al.*, *Science* **250**, 1426–1429 (1990).
7. A. A. Ferrando *et al.*, *Blood* **103**, 1909–1911 (2004).
8. K. Leroy-Viard, M. A. Vinit, N. Lecointe, D. Mathieu-Mahul, P. H. Roméo, *Blood* **84**, 3819–3827 (1994).
9. T. Sanda *et al.*, *Cancer Cell* **22**, 209–221 (2012).
10. M. R. Mansour *et al.*, *J. Exp. Med.* **210**, 1545–1557 (2013).
11. R. Siersbæk *et al.*, *Cell Rep.* **7**, 1443–1455 (2014).
12. J. Lovén *et al.*, *Cell* **153**, 320–334 (2013).
13. P. Filippakopoulos *et al.*, *Nature* **468**, 1067–1073 (2010).
14. S. C. Parker *et al.*, *Proc. Natl. Acad. Sci. U.S.A.* **110**, 17921–17926 (2013).
15. D. Hnisz *et al.*, *Cell* **155**, 934–947 (2013).
16. W. A. Whyte *et al.*, *Cell* **153**, 307–319 (2013).
17. N. Kwiatkowski *et al.*, *Nature* **511**, 616–620 (2014).
18. Y. Zhou *et al.*, *Blood* **122**, 4199–4209 (2013).
19. D. E. Newburger, M. L. Bulyk, *Nucleic Acids Res.* **37** (Database), D77–D82 (2009).
20. P. Dai *et al.*, *Genes Dev.* **10**, 528–540 (1996).
21. F. Tie *et al.*, *Development* **141**, 1129–1139 (2014).
22. C. Schulz *et al.*, *Science* **336**, 86–90 (2012).
23. A. Rada-Iglesias *et al.*, *Nature* **470**, 279–283 (2011).
24. M. P. Creyghton *et al.*, *Proc. Natl. Acad. Sci. U.S.A.* **107**, 21931–21936 (2010).

ACKNOWLEDGMENTS

We thank J. Gilbert for helpful editorial comments on the manuscript, J. Reddy for sharing data, and F.Alt and F. Meng for helpful advice on the design of the CRISPR experiments. We would like to dedicate this paper to the memory of Michael Fayngersh. We gratefully acknowledge the children with T-ALL and their families for the samples analyzed in these studies. M.R.M. was supported by the Claudia Adams Barr Innovative Basic Science Research Program, the Kay Kendall Leukaemia Trust, and a Bennett Fellowship from Leukaemia and Lymphoma Research, UK. A.G. is a Research Fellow of the Gabrielle's Angel Foundation for Cancer Research, a Clinical Investigator of the Damon Runyon Cancer Research Foundation, and is supported by grants National Cancer Institute, NIH, CA167124, Department of Defense, CA120215 and an award from the William Lawrence and Blanche Hughes Foundation. T.S. is supported by a grant from the National Research Foundation (NRF), Prime Minister's Office, Singapore under its NRF Fellowship Program (award no. NRF-NRFF2013-02). This work was funded by NIH grants 1R01CA176746-01 and 5P01CA109901-08 (A.T.L.), and 5P01CA68484 (S.E.S. and A.T.L.). Children's Oncology Group cell banking and sample distribution were supported by grants CA98543, CA114766, CA98413, CA30969, and CA29139 from the NIH. S.P.H. is the Ergen Family Chair in Pediatric Cancer. R.A.Y. is a founder and member of the Board of Directors of Syros Pharmaceuticals, a company developing therapies that target gene regulatory elements including super-enhancers.

SUPPLEMENTARY MATERIALS

www.sciencemag.org/content/346/6215/1373/suppl/DC1
Materials and Methods
Figs. S1 to S9
Tables S1 to S3
References (*25*–*44*)

22 July 2014; accepted 4 November 2014
Published online 13 November 2014;
10.1126/science.1259037

ELECTRON MICROSCOPY

Ultrastable gold substrates for electron cryomicroscopy

Christopher J. Russo and Lori A. Passmore*

Despite recent advances, the structures of many proteins cannot be determined by electron cryomicroscopy because the individual proteins move during irradiation. This blurs the images so that they cannot be aligned with each other to calculate a three-dimensional density. Much of this movement stems from instabilities in the carbon substrates used to support frozen samples in the microscope. Here we demonstrate a gold specimen support that nearly eliminates substrate motion during irradiation. This increases the subnanometer image contrast such that α helices of individual proteins are resolved. With this improvement, we determine the structure of apoferritin, a smooth octahedral shell of α-helical subunits that is particularly difficult to solve by electron microscopy. This advance in substrate design will enable the solution of currently intractable protein structures.

Recent developments in electron cryomicroscopy (cryo-EM) have allowed structure determination to near-atomic resolution for some macromolecular complexes (*1*–*3*). Still, many small and challenging structures cannot be determined by current cryo-EM methods to the resolutions required for accurate modeling of atom positions. This is because electron micrograph quality still falls short of the physical limits imposed by radiation damage to the macromolecules (*4*–*6*). Reduced image quality likely has two primary origins: inefficient detection of imaging electrons (*6*, *7*) and motion and blurring of the particles during irradiation (*6*, *8*–*11*). Recent developments in electron detectors have addressed the first constraint (*12*, *13*) and have enabled the development of motion correction algorithms to ameliorate the effects of the second (*14*–*16*). Direct electron detectors can acquire images using fractions of the electron dose previously required, thus allowing the measurement of single-molecule positions in time. This allows accurate tracking of large ensembles of particles and offers a way to determine the physical origins of radiation-induced particle movement (*14*–*17*).

Medical Research Council (MRC) Laboratory of Molecular Biology, Francis Crick Avenue, Cambridge CB2 0QH, UK.
*Corresponding author. E-mail: passmore@mrc-lmb.cam.ac.uk

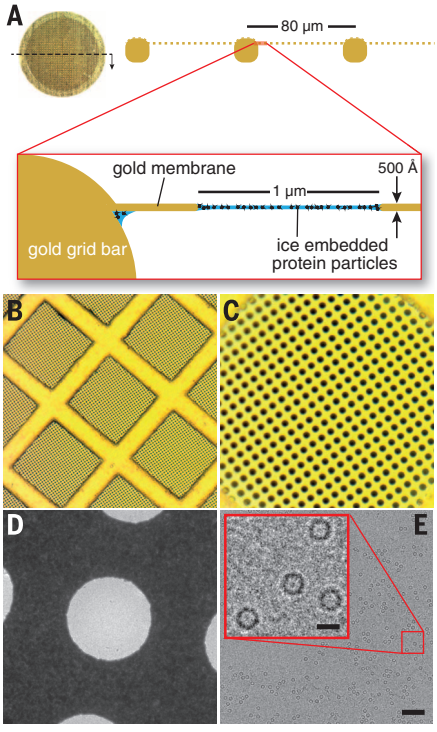

Fig. 1. Ultrastable substrate design. The ultrastable gold support comprises a 3-mm diameter disc of gold mesh (A) where a ≅500 Å thick layer of gold foil with a regular array of micrometer-sized holes is suspended across the square openings in the mesh (diagramed along the section indicated). After application of an aqueous protein sample and plunge freezing at ≅80 K, each hole contains a thin film of protein particles embedded in vitrified ice. (**A** to **C**) Optical micrographs of the gold grid at low, medium, and high magnification respectively; each hole is 1.2 μm in diameter and sets the scale for (B) to (D). (**D**) Transmission electron micrograph of an individual 1.2-μm hole containing vitrified ice. (**E**) A typical high-resolution electron micrograph of apoferritin suspended in ice on a gold grid. Scale bars for the micrograph and magnified inset are 1200 and 120 Å, respectively.

Conventional amorphous carbon (am-C) substrates undergo bending and deformation during irradiation (*9*, *11*), which includes movement both parallel and perpendicular to the substrate plane. Incorporation of titanium-silicon, doped silicon carbide, or graphene into substrate designs reduced radiation-induced specimen motion (*17*–*19*). Still, these designs did not stop substrate movement and are challenging to manufacture and use. Here we demonstrate a cryo-EM support that nearly eliminates the radiation-induced deformation of thin, ice-embedded specimens at cryogenic temperatures. This curtails the perpendicular and in-plane components of motion during imaging and thus improves image quality for all radiation-sensitive cryogenic specimens.

The support comprises a regular array of micrometer-sized holes in a ≅500 Å thick foil of gold (Fig. 1 and fig. S1; see also supplementary materials and methods). The foil is suspended across a mesh grid, also composed of gold, with square holes ≅80 μm wide. It differs from standard am-C supports only in the choice of materials and the thickness of the perforated foil. We chose gold because it is a highly conductive, nonoxidizing, radiation-hard material whose surface is chemically inert and biocompatible. Furthermore, making the foil and grid entirely out of the same metal ensures uniform electrical conductivity and prevents differential thermal contraction during cooling from 300 to 80 K, thus maintaining the geometry and tension of the support foil during use.

To characterize performance, we first measured the vertical motion of tilted gold substrates, without ice, under irradiation using standard cryogenic conditions (Fig. 2A and movie S1). Compared with commercial am-C supports with nearly identical geometry, there was a 60-fold reduction in substrate displacement (228 versus 3.8 Å) in a typical fluence used for high-resolution cryo-EM (16 e^-/Å^2). Next, we compared the vertical motion of the gold and am-C substrates when supporting a typical layer of thin ice used to image proteins (Fig. 2B). Adding the layer of ice stabilized both the am-C and gold supports, but there was still a 40-fold reduction in movement on gold compared with am-C (76 versus 1.9 Å).

To characterize the in-plane motion (parallel to the plane of the support) of proteins suspended in ice on gold substrates, we made test samples using 80*S* ribosomes and tracked them under standard imaging conditions. We analyzed a large ensemble of particle trajectories and compared these to previously published data on other substrates (Fig. 3A and fig. S2) (*17*). Particles generally exhibit two phases of motion during irradiation—a faster phase during the first 4e^-/Å^2 followed by a slower phase—and both are significantly reduced using gold (by ≅40% and ≅80%, respectively). This shows that much of the first phase and most of the second phase of particle motion are due to the support. On the gold substrate, the signal in the second part of the exposure approaches the physical limits imposed by damage and detector efficiency (fig. S3). Based on these experiments, we posit that reducing the vertical motion of the support by 50-fold reduces the total in-plane motion of the particles by twofold, where the coupling between the vertical and in-plane motion is due to bending of the irradiated region. We include a model of substrate deformation accounting for this in the supplement (fig. S4).

A reduction in motion directly improves the quality of the images. We quantify this using statistical analysis of tilt-pair images of ribosomes (*20*) collected on the different supports (fig. S5). These data demonstrate a 140% improvement in κ, which is a direct measure of the quality of the images. This corresponds to a 35% improvement in the accuracy of the angles assigned to the individual images during three-dimensional (3D) reconstruction (fig. S5C), which is crucial for solving macromolecular structures. Given a high-quality protein preparation, angular accuracy and the isotropic coverage of the information content in Fourier space are the primary factors that determine whether and how accurately a structure can be determined by cryo-EM.

To further assess the performance of gold supports, we determined the structure of apoferritin, a small protein (18 kD) that assembles into a

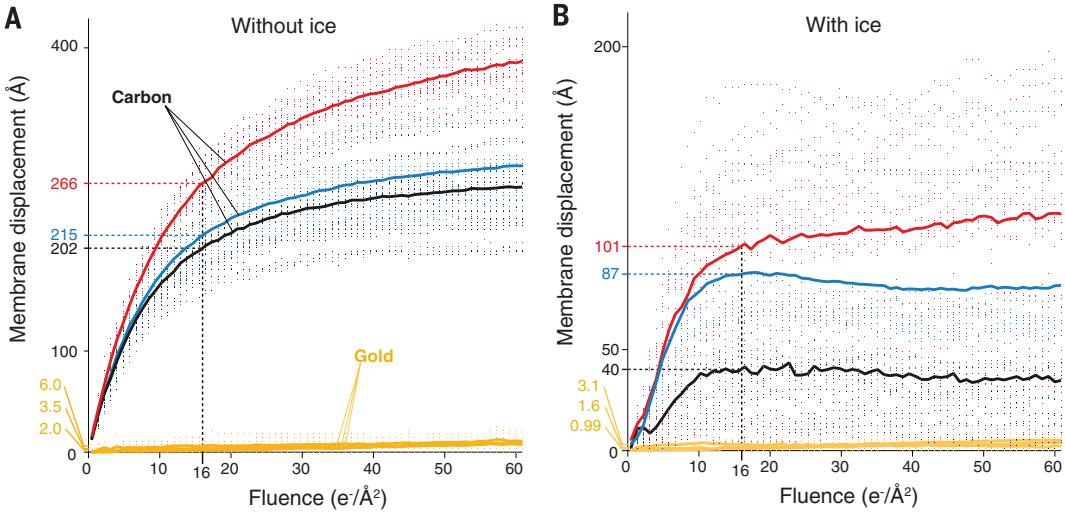

Fig. 2. Reduced motion of gold substrates under high-energy electron irradiation. (**A**) Measurements of the vertical motion of am-C and gold supports under typical cryo-EM illumination conditions (300 keV, 16 e^-/Å^2 per second, and 80 K). Each point is the magnitude of vertical displacement of the edge of a particular hole in the foil relative to its initial position before electron irradiation. Each solid line is the root mean square displacement for multiple holes in multiple squares of one grid. When a typical thin layer of vitreous ice is present (**B**), the vertical motion of both substrates is reduced about twofold, and the motion on am-C becomes more complicated in nature.

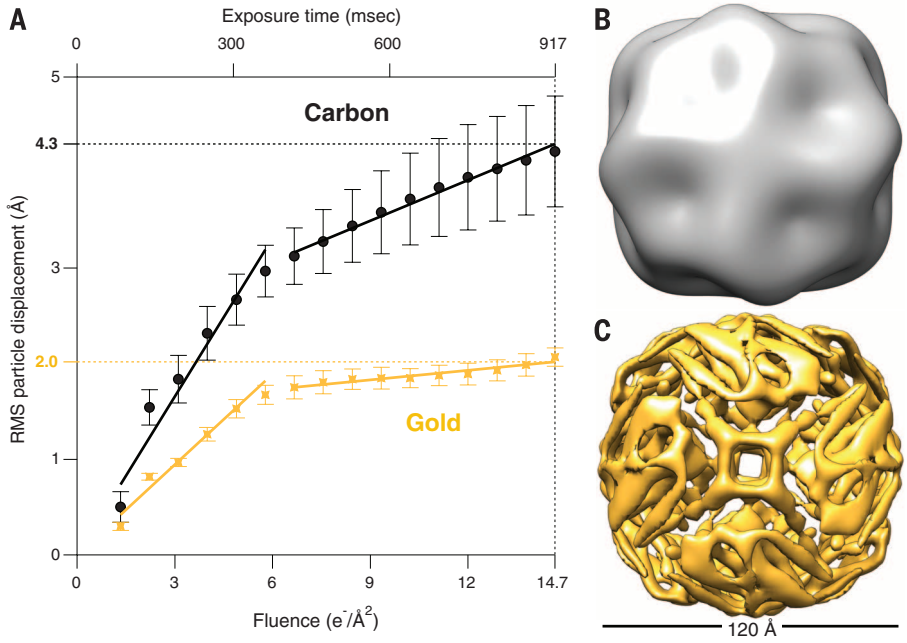

Fig. 3. Reduced particle motion and improved resolution on ultrastable grids. (**A**) 80*S* ribosomes were tracked during electron irradiation (using the same imaging conditions) for particles supported on three different am-C grids [black circles (*17*)] and three different gold grids (gold crosses). Each point is the in-plane ensemble average displacement of a particle from its initial position, and the error bars denote the SEM for the multiple grids tested. RMS, root mean square. Solid lines are linear fits to the two phases of motion, where the slopes are the average speeds of the particles. There was a 43% reduction in the speed of the first phase (8.8 to 5.0 Å/s) and a 77% reduction in the speed of the second phase (2.3 to 0.53 Å/s) on gold relative to am-C. Density maps of apoferritin processed identically from data collected using identical conditions for am-C (**B**) and gold (**C**) substrates. The map in (B) has a resolution of 25 Å (gold-standard Fourier shell correlation) and contains no discernible information beyond that present in the initial model. Compare to (C) with a resolution of 8.0 Å, which resolves the entire molecular chain.

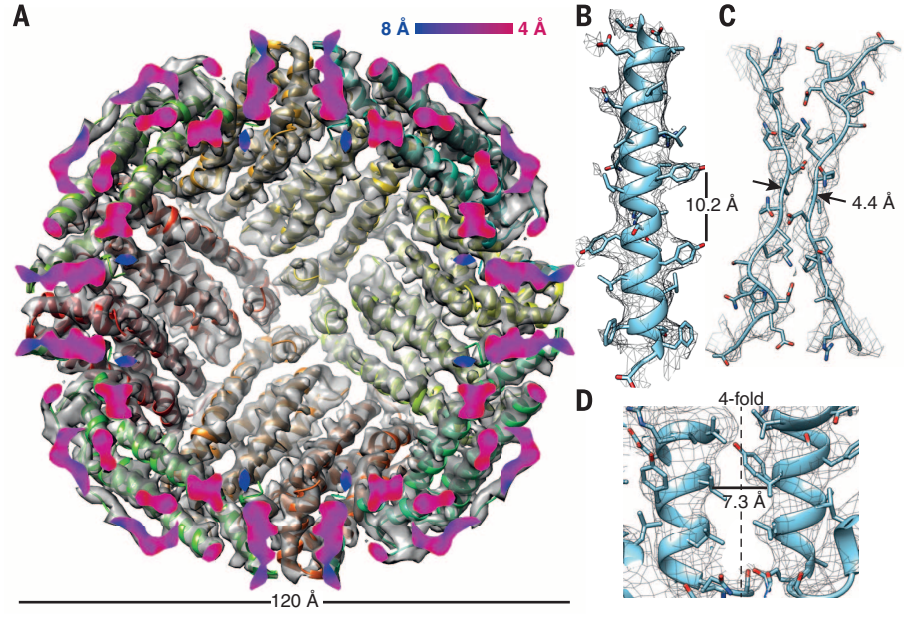

Fig. 4. The structure of apoferritin from 483 single-particle images. (**A**) The previously published x-ray crystal structure is fit to the cryo-EM density map, and the density is cut in half along the plane defined by two of the fourfold symmetry axes to reveal the interior of the complex. The cut surface shows the local resolution of the density using the color scale as indicated. (**B**) View of one of the α helices showing clear side-chain density. (**C**) View along the twofold symmetry axis showing clear separation between the β strands. (**D**) Section parallel to the fourfold pore axis showing the corrugated density of the residues in the interior of the pore.

smooth, spherical complex (440 kD). The ferritins are a class of iron-storage proteins that are conserved throughout evolution and whose characteristic structural motif is a bundle of four α helices (*21*, *22*). Apoferritin has remained intractable to structure determination by cryo-EM—even using the new generation of electron detectors—because the contrast in individual particle images was insufficient for the resolution of α helices, which is required to align the images with each other (*6*, *23*). We collected data on gold and am-C supports prepared identically (with identical geometry and imaging conditions, on the same day, and on the same microscope equipped with a back-thinned direct electron detector) and processed the resulting 4000 particles from each support type identically (Fig. 3, B and C). The images of apoferritin on am-C are still too blurred for correct alignment, resulting in a 3D density map that is no better than the initial model (resolution ≃25 Å); the reduced motion of the proteins on the gold grids improves the images enough that the orientations are correctly assigned, yielding a map that resolves the entire molecular chain (≃8 Å).

We used the gold support to collect a larger data set of ≃6000 particles. This yielded a reconstruction with a resolution of ≃7 Å (fig. S6). We suspected that conformational heterogeneity was limiting the resolution of the reconstruction. Using 3D classification (*24*), we were able to isolate a subset of 483 particles (11,592 asymmetric units) where a flexible loop on the exterior of the complex was positioned along the dimer interface, although we cannot exclude the possibility that the classification process may also have selected for particles that happened to move less during imaging. This improved the map (Fig. 4) and brought the resolution of the reconstruction to 4.7 Å (fig. S7).

The final map shows clearly identifiable density for the larger side chains, distinct separation of the β strands along the dimerization interface, and the molecular surface within the pore along the fourfold axis (Fig. 4, B to D). We found a region of extra density at the C terminus (fig. S8) corresponding to three amino acids in the protein sequence that were not modeled in the crystal structure (*25*). Refinement of an atomic model against the map also suggests an alternate conformation of the molecule relative to the crystal structure (fig. S7A).

The improved stability and image quality of gold substrates is not due to the mechanical strength of the suspended foil (fig. S9) but instead is likely due to preservation of the tension in the membrane during the cooling process, combined with the radiation hardness and high conductivity of the gold film at cryogenic temperatures. Substrates that reduce radiation-induced motion will improve the images from every microscope, not just those equipped with a direct electron detector or high-speed frame capture hardware and processing algorithms. We expect that the 50-fold reduction in the vertical motion of the gold substrates will also enable electron tomography at increased resolutions, as images of tilted specimens are more severely affected by the vertical motion of the substrate. The methods herein will allow one to solve the structures of many proteins previously refractory

to structural analysis, including other ferritins that could not be solved by x-ray crystallography.

During the first 4 $e^-/Å^2$ on gold substrates, 1 to 2 Å of in-plane motion remain. These first few electrons are critical, as they potentially contain the most high-resolution information (*26*, *27*). Future work will focus on substrate design and image acquisition conditions to reduce the initial motion even more. Along with further improvements in electron detector efficiency, this will bring cryo-EM to the physical limits imposed by the homogeneity of the protein preparation, the electron scattering cross sections of the biological specimen (*4*), and the counting statistics of detecting individual electrons. We anticipate that high-efficiency, stationary particle imaging will allow: (i) measurement and modeling of the progressive damage to the primary and secondary structure of the molecules, (ii) improved refinements using dose-fractionation that includes the use of tilt, and (iii) direct modeling and refinement of molecular structure from particle images. This will enable routine structure determination for many molecules and complexes that are currently too difficult to be practical.

REFERENCES AND NOTES

1. A. Amunts *et al.*, *Science* **343**, 1485–1489 (2014).
2. M. Liao, E. Cao, D. Julius, Y. Cheng, *Nature* **504**, 107–112 (2013).
3. M. Allegretti, D. J. Mills, G. McMullan, W. Kühlbrandt, J. Vonck, *eLife* **3**, e01963–e01963 (2014).
4. R. Henderson, *Q. Rev. Biophys.* **28**, 171–193 (1995).
5. P. B. Rosenthal, R. Henderson, *J. Mol. Biol.* **333**, 721–745 (2003).
6. R. Henderson, G. McMullan, *Microscopy* **62**, 43–50 (2013).
7. A. Faruqi, R. Henderson, M. Pryddetch, P. Allport, A. Evans, *Nucl. Instrum. Methods* **546**, 170–175 (2005).
8. R. Henderson, R. M. Glaeser, *Ultramicroscopy* **16**, 139–150 (1985).
9. E. R. Wright, C. V. Iancu, W. F. Tivol, G. J. Jensen, *J. Struct. Biol.* **153**, 241–252 (2006).
10. R. M. Glaeser, G. McMullan, A. R. Faruqi, R. Henderson, *Ultramicroscopy* **111**, 90–100 (2011).
11. A. F. Brilot *et al.*, *J. Struct. Biol.* **177**, 630–637 (2012).
12. G. McMullan, S. Chen, R. Henderson, A. R. Faruqi, *Ultramicroscopy* **109**, 1126–1143 (2009).
13. G. McMullan, A. R. Faruqi, D. Clare, R. Henderson, *Ultramicroscopy* **147**, 156–163 (2014).
14. M. G. Campbell *et al.*, *Structure* **20**, 1823–1828 (2012).
15. X.-C. Bai, I. S. Fernandez, G. McMullan, S. H. Scheres, *eLife* **2**, e00461 (2013).
16. X. Li *et al.*, *Nat. Methods* **10**, 584–590 (2013).
17. C. J. Russo, L. A. Passmore, *Nat. Methods* **11**, 649–652 (2014).
18. D. Rhinow, W. Kühlbrandt, *Ultramicroscopy* **108**, 698–705 (2008).
19. C. Yoshioka, B. Carragher, C. S. Potter, *Microsc. Microanal.* **16**, 43–53 (2010).
20. C. J. Russo, L. A. Passmore, *J. Struct. Biol.* **187**, 112–118 (2014).
21. S. H. Banyard, D. K. Stammers, P. M. Harrison, *Nature* **271**, 282–284 (1978).
22. R. R. Crichton, J.-P. Declercq, *Biochim. Biophys. Acta* **1800**, 706–718 (2010).
23. W. H. Massover, *Micron* **24**, 389–437 (1993).
24. S. H. W. Scheres, *J. Struct. Biol.* **180**, 519–530 (2012).
25. N. de Val, J.-P. Declercq, C. K. Lim, R. R. Crichton, *J. Inorg. Biochem.* **112**, 77–84 (2012).
26. W. Baumeister, M. Hahn, J. Seredynski, L. M. Herbertz, *Ultramicroscopy* **1**, 377–382 (1976).
27. H. Stark, F. Zemlin, C. Boettcher, *Ultramicroscopy* **63**, 75–79 (1996).

ACKNOWLEDGMENTS

We thank R. Henderson for guidance and advice throughout this project; D. Mills and W. Kühlbrandt for the use of the Polara electron microscope at the Max Planck Institute of Biophysics, Frankfurt; I. S. Fernandez and the V. Ramakrishnan lab for the gift of ribosomes; G. McMullan, S. Chen, C. Savva, J. Grimmett, T. Darling, and M. Skehel for technical assistance; our colleagues at the Laboratory of Molecular Biology—especially S. Scheres, G. Murshudov, and R. A. Crowther—for many helpful discussions; and R. A. Crowther, V. Ramakrishnan, and E. Rajendra for a critical reading of the manuscript. This work was supported by the European Research Council (ERC) under the European Union's Seventh Framework Programme (FP7/2007-2013)/ERC grant agreement no. 261151 and MRC grant U105192715. C.J.R. and L.A.P. are inventors on a patent application filed by the MRC on the gold substrates. The coordinates of the refined apoferritin model are deposited in the Protein Data Bank under accession code 4v1w and the EM density map is deposited in the Electron Microscopy Database under accession code 2788.

SUPPLEMENTARY MATERIALS

www.sciencemag.org/content/346/6215/1377/suppl/DC1
Materials and Methods
Figs. S1 to S10
Table S1
References (*28*–*40*)
Movie S1

4 August 2014; accepted 13 November 2014
10.1126/science.1259530

HIV ANTIBODIES

Antigen modification regulates competition of broad and narrow neutralizing HIV antibodies

Andrew T. McGuire,[1]*† Anita M. Dreyer,[1]*‡ Sara Carbonetti,[1] Adriana Lippy,[1] Jolene Glenn,[1]† Johannes F. Scheid,[2] Hugo Mouquet,[3] Leonidas Stamatatos[1,4]†§

Some HIV-infected individuals develop broadly neutralizing antibodies (bNAbs), whereas most develop antibodies that neutralize only a narrow range of viruses (nNAbs). bNAbs, but not nNAbs, protect animals from experimental infection and are likely a key component of an effective vaccine. nNAbs and bNAbs target the same regions of the viral envelope glycoprotein (Env), but for reasons that remain unclear only nNAbs are elicited by Env immunization. We show that in contrast to germline-reverted (gl) bNAbs, glnNAbs recognized diverse recombinant Envs. Moreover, owing to binding affinity differences, nNAb B cell progenitors had an advantage in becoming activated and internalizing Env compared with bNAb B cell progenitors. We then identified an Env modification strategy that minimized the activation of nNAb B cells targeting epitopes that overlap those of bNAbs.

During HIV-1 infection, the viral envelope glycoprotein (Env) elicits a polyclonal antibody response that targets diverse epitopes (*1*, *2*). Antibodies that display narrow breadth of neutralization (narrow neutralizing antibodies; nNAbs) develop during the first months of infection whereas those capable of neutralizing heterologous viruses (broadly neutralizing antibodies; bNAbs) develop several years later in ~10 to 30% of HIV-1–positive individuals (*3*). bNAbs isolated from HIV-1–infected patients are more protective than nNAbs in experimental HIV-1/SHIV infection (*4*) and will likely be a key component of an effective HIV-1 vaccine. Even though nNAbs and bNAbs target the same regions of Env (*2*, *5*–*7*), recombinant Env (rEnv) immunogens are poorly recognized by germline-reverted (gl) bNAbs (glbNAbs) and their corresponding B cell receptors (BCRs) (*5*, *8*–*21*), suggesting that the lack of bNAb generation during immunization may be due to inefficient stimulation of naïve bNAb BCR progenitors (*17*, *20*). In contrast, little is known about the recognition of rEnv by the naïve BCR progenitors of nNAbs. Understanding why B cell responses against nNAb epitopes dominate over those targeted by bNAbs in the context of rEnv immunization will inform on basic immunological mechanisms of epitope competition and provide new information relevant to the development of an effective HIV-1 vaccine.

Here we investigated whether glnNAbs from distinct clonal lineages that targeted the CD4-binding site (BS) and V3 regions of Env (*2*) also display minimal rEnv recognition. Amino acid differences between the mutated and gl sequences of nNAbs range from 2.4 to 7.3% for the heavy chains and 2.7 to 5.6% for the light chains for the nNAb CD4-BS antibodies (table S1 and fig. S1). In contrast, prototypic CD4-BS bNAbs, VRC01 (33.9% heavy, 23% light), NIH45-46 (a clonal relative of VRC01; 39.8% heavy, 26.1% light), b12 (21% heavy, 19% light), 8ANC131 (33% heavy, 24% light), and CH103 (12.7% heavy, 10% light) are more mutated (*5*, *8*, *16*, *22*). The anti-V3 nNAbs are more mutated (11.6 to 21.6% heavy, 9.7 to 13.8% light) than the anti-CD4-BS nNAbs.

In contrast to the anti-CD4-BS glbNAbs, which do not bind rEnv (*5*, *8*, *16*, *17*, *20*) (table S2), glnNAbs displayed broad Env recognition (from 51 to 100%) (table S2). The binding affinities of the glnNAbs were generally weaker than those of the corresponding mutated antibodies, owing to increased off rates in most cases (fig. S2).Whereas the glVRC01 class bNAbs were unable to neutralize any of the

[1]Seattle Biomedical Research Institute, Seattle, WA 98109, USA. [2]Laboratory of Molecular Immunology, The Rockefeller University, New York, NY 10065, USA. [3]Laboratory of Humoral Response to Pathogens, Department of Immunology, Institut Pasteur and CNRS-URA 1961, 75015 Paris, France. [4]Department of Global Health, University of Washington, Seattle, WA 98109, USA.
*These authors contributed equally to this work. †Present address: Fred Hutchinson Cancer Research Center, Seattle, WA 98109, USA. ‡Present address: GlycoVaxyn, Grabenstrasse 3, CH-8952 Schlieren, Switzerland. §Corresponding author. E-mail: lstamata@fhcrc.org

Science
AAAS

Ultrastable gold substrates for electron cryomicroscopy

Christopher J. Russo and Lori A. Passmore

Science **346**, 1377 (2014);
DOI: 10.1126/science.1259530

Science (print ISSN 0036-8075; online ISSN 1095-9203) is published weekly, except the last week in December, by the American Association for the Advancement of Science, 1200 New York Avenue NW, Washington, DC 20005.